Nitro-substituted ruthenium(II) polypyridyl complexes synergise with ATR inhibitors to enhance replication stress in cancer cells

Yian Chee Gan[1,‡], Nur Aininie Yusoh[2,‡], Suet Lin Chia[3,4,5], Xiaohe Tian[2,*], Martin R. Gill[6,*] and Haslina Ahmad[1,4*]

[1]Department of Chemistry, Faculty of Science, Universiti Putra Malaysia, 43400 UPM Serdang, Selangor, Malaysia

[2]Department of Radiology, Huaxi MR Research Center (HMRRC), Institute of Radiology and Medical Imaging, West China Hospital of Sichuan University, Sichuan University, Chengdu, Sichuan, China

[3]Department of Microbiology, Faculty of Biotechnology and Biomolecular Science, Universiti Putra Malaysia, 43400 UPM Serdang, Selangor, Malaysia

[4]UPM-MAKNA Cancer Research Laboratory, Institute of Bioscience, Universiti Putra Malaysia, 43400 UPM Serdang, Selangor, Malaysia

[5]Malaysia Genome and Vaccine Institute, National Institutes of Biotechnology Malaysia, Jalan Bangi, 43000 Kajang, Malaysia

[6]Department of Chemistry, Faculty of Science and Engineering, Swansea University, Swansea, UK

Email: xiaohe.t@wchscu.cn, m.r.gill@swansea.ac.uk and haslina_ahmad@upm.edu.my

[‡]These authors contributed equally to the work.

Abstract

Ruthenium(II) polypyridyl complexes (RPCs) are promising anticancer candidates owing to their ability to intercalate DNA and disrupt DNA replication. Here, we report a series of nitro-substituted ruthenium(II) complexes of general formula $[Ru(dppz)_2(NPIP)]^{2+}$ (dppz = dipyridophenazine; NPIP = 2-(nitrophenyl)imidazo[4,5-*f*][1,10]phenanthroline), in which systematic positional tuning of the nitro substituent (*ortho*, *meta*, *para*) modulates DNA reactivity and biological activity. All three isomers retain the characteristic MLCT

photophysical properties of the Ru-dppz core and intercalate DNA with high affinity, while exhibiting distinct membrane-associated localisation in cancer cells. Despite limited nuclear accumulation, the complexes induce pronounced ROS-mediated DNA damage and display selective cytotoxicity towards cancer cells over normal fibroblasts. The nitro-substituted complexes demonstrated an enhanced DNA double-strand break (DSB) cellular response in the form of ATM pathway activation and γH2AX foci generation compared to the parent complex $[Ru(dppz)_2(PIP)]^{2+}$ (PIP = 2-(phenyl)imidazo[4,5-*f*][1,10]phenanthroline). Among them, the para-substituted nitro derivative (complex **3**) induces the strongest DNA damage response and was therefore investigated in combination with the ATR inhibitors (ATRi) berzosertib and ceralasertib. Strong synergism is observed across multiple cancer cell lines, with combination treatment markedly suppressing clonogenic survival and enhancing DNA damage signalling and apoptotic cell death. Mechanistic analyses reveal that DNA intercalation and reactive oxygen species (ROS) generation cooperatively elevate replication stress, driving ATR-dependent survival and sensitizing cells to DDR-targeted therapy. Comparable ATRi synergism was also observed for the parent complex Ru-PIP. This study demonstrates that positional nitro substitution of the Ru-PIP scaffold offers a means to fine-tune DNA-binding behaviour and the resulting DNA damage response, and that Ru(II) metallointercalators can mechanistically synergize with ATR inhibition, introducing a new strategy for combining metal-based DNA binders with precision DDR therapeutics.

Keywords: Ruthenium(II) complexes; DNA damage response (DDR); ATR inhibition; Drug synergy; Replication stress; Cancer therapy

Introduction

Metal-based complexes have gained significant attention as anticancer agents due to their distinctive photophysical characteristics, redox tunability, and structural adaptability, which enable precise modulation of nucleic acids and proteins in living systems.[1-5] Following the clinical success of platinum-based cisplatin, ruthenium(II) polypyridyl complexes have emerged as promising metallodrugs with therapeutic potential.[6-10] In addition to their cytotoxic properties, ruthenium complexes have been widely explored as luminescent probes for cellular and molecular imaging applications.[11-14] Previously, we reported the ruthenium(II)

metallointercalator $[Ru(dppz)_2(PIP)]^{2+}$ (dppz = dipyridophenazine, PIP = 2-(phenyl)imidazo[4,5-*f*][1,10]phenanthroline; hereafter Ru-PIP), binds DNA with high affinity, induces replication fork stalling, and activates DNA damage response (DDR) signalling, as evidenced by checkpoint kinase 1 (Chk1) phosphorylation and G1-S phase arrest without directly causing double-strand breaks (DSBs) or apoptosis under basal conditions.[15] Its sterically bulky ligands create a physical barrier to replication fork progression, establishing Ru-PIP as a replication stress inducer. Since replication stress is a molecular hallmark of cancer and a key therapeutic vulnerability, agents that impede DNA synthesis and activate the DDR can selectively target tumour cells while sparing healthy normal cells. Building on this background, we aimed to modify the Ru-PIP complex, particularly by introducing electronic modifications to further optimize its therapeutic potential. Specifically, nitro substitution was selected as an electron-withdrawing modification capable of altering π-π stacking propensity, redox potential, and bioreductive reactivity without disrupting the coordination geometry of the parent scaffold.

Tumour hypoxia, a common feature of solid malignancies, significantly influences cancer progression, therapeutic resistance, and immune evasion.[15] Hypoxic adaptation reprograms cellular metabolism and signalling, thereby diminishing the efficacy of chemotherapy, radiotherapy, and immunotherapy. Nitro ($-NO_2$) substituents, being strongly electron-withdrawing, influence π-π stacking interactions and undergo enzymatic reduction under hypoxic conditions to yield reactive intermediates capable of inducing oxidative stress or forming covalent adducts with DNA and proteins.[16] Building on these properties, we hypothesized that electronic modulation of the PIP ligand via nitro substitution could modulate its biological activity and enable selective activation in cancer cells. In this study, we investigate how these electronic modifications impact the therapeutic potential of the ruthenium complexes. Indeed, nitro-functionalised ruthenium complexes have been reported to display enhanced anticancer activity, including under hypoxic conditions, highlighting the functional relevance of this electronic modification.[17-19]

Single-agent therapies are often limited by dose-limiting toxicity and the emergence of resistance, whereas rational drug combinations can achieve effects greater than the sum of their parts, allowing lower dosing and reducing systemic burden.[20, 21] Metal complexes have shown notable synergy with other drugs.[22, 23] Ru-PIP, for instance, has been reported to

potentiate the PARP inhibitor olaparib, consistent with its ability to induce replication stress and activate DDR pathways,[24, 25] underscoring its potential in combination regimens that exploit replication stress. Other ruthenium complexes have shown synergy with gemcitabine,[26] doxorubicin,[27, 28] sorafenib,[29] erlotinib,[30] reforafenib,[31] and paclitaxel,[32] underscoring the broad potential of Ru-based combination strategies. Here, we focus on synergy with ataxia telangiectasia and Rad3-related (ATR) kinase inhibitors. ATR is a central DDR regulator that senses replication stress, activates cell-cycle checkpoints, and maintains genomic stability. Inhibiting ATR prevents stabilization of stalled forks, leading to DSB accumulation, incomplete replication, and mitotic catastrophe.[33-35] Several ATR inhibitors (ATRi) such as berzosertib, ceralasertib, elimusertib, gartisertib, and tuvusertib, are currently under clinical evaluation, including in combination with DNA-damaging or DDR-targeted agents.[36-38] ATR inhibitors have shown synergy with PARP inhibitors, reflecting the therapeutic advantage of targeting complementary DDR pathways.[39-42] The mechanistic overlap between Ru-PIP and ATR inhibition suggests that dual treatment could overwhelm DNA repair capacity and induce apoptosis through a synthetic lethal mechanism.

While ruthenium(II) polypyridyl complexes, particularly dppz-based metallointercalators, have been extensively investigated as DNA-targeting agents,[24, 25, 43] the translation of replication-stress-inducing Ru complexes into rational DNA damage response (DDR) combination strategies remains underexplored. In particular, evaluation of their synergy with ATR inhibition, a central mediator of replication stress tolerance,[44] has not been previously established. This gap provides an opportunity to exploit chemically induced replication stress using clinically relevant checkpoint inhibitors.

In this study, we report the design and characterization of nitro-substituted $[Ru(dppz)_2(NPIP)]^{2+}$ complexes (NPIP = 2-(nitrophenyl)imidazo[4,5-*f*][1,10]phenanthroline) and examine how positional nitro substitution on the PIP ligand the PIP ligand influences DNA binding and cellular responses. We demonstrate that these complexes induce replication stress through DNA intercalation and ROS generation. This replication-associated stress can be effectively exploited using clinically relevant ATR inhibitors. The resulting synergistic activity highlights a rational strategy for combining metal-based DNA-interacting agents with DDR-targeted therapies for cancer treatment.

Experimental

Materials and reagents

$[Ru(dppz)_2(PIP)]^{2+}$ (Ru-PIP) was synthesized and purified as previously reported.[43] Antibodies for total ATM, cleaved caspase-3, β-actin, and GAPDH were purchased from Proteintech. Antibodies for phospho-ATM (Ser1981) were obtained from Affinity Biosciences. Antibodies for γH2AX (Ser139) and singlet oxygen sensor green (SOSG) were purchased from Beyotime. Horseradish peroxidase (HRP)-conjugated secondary antibodies, N-acetylcysteine (NAC) and berzosertib were purchased from MedChemExpress. 2',7'-Dichlorodihydrofluorescein diacetate (DCFH-DA) was obtained from Solarbio. Ceralasertib was obtained from Targetmol, USA, CellMask Deep Red from Invitrogen and DAPI were obtained from Sigma Aldrich. Unless otherwise noted, all other chemicals were purchased from Sigma-Aldrich or ThermoFisher Scientific and used without further purification. Stock solutions of berzosertib and ceralasertib (1 mM) were prepared in 100% dimethyl sulfoxide (DMSO) and stored at -20 °C. NAC stock solutions (10 mM) were prepared in phosphate-buffered saline (PBS). Stock solutions were diluted in PBS or DMEM for experiments, with a final DMSO concentration ≤ 0.1%.

Characterisation of complexes

^1H NMR spectra were recorded on an Agilent VNMRJ 500 MHz NMR spectrometer. ESI-MS was recorded using Thermo Scientific LTQ Orbitrap XL mass spectrometer. Fourier-transform infrared (FT-IR) spectra were recorded on a PerkinElmer Spectrum 100 Series FTIR Spectrometer. Elemental analyses were performed by the Thermo Scientific FlashSmart CHNS/O Elemental Analyzer at Universiti Kebangsaan Malaysia (UKM).

Synthesis of $[Ru(dppz)_2(NPIP)]^{2+}$ complexes

Complexes **1**-**3** were synthesized following an adapted literature procedure.[43, 45] $Ru(dppz)_2(Cl)_2$ was reacted with equimolar amounts of NPIP in dry ethylene glycol under nitrogen reflux for 4 h. After cooling, KPF_6 was added, and the precipitate was collected, washed with distilled water, and dried under vacuum. Crude products were purified by alumina column chromatography using 1:1 acetonitrile/toluene. Reddish-orange fractions were collected and dried in vacuo.

Complex **1**: Mass (Yield): 0.122 g (49.5%). ^{1}H NMR (CD_3CN, δ ppm): 9.66 (d, *J* = 8.1 Hz, 2H), 9.62 (d, *J* = 8.1 Hz, 2H), 8.91 (d, *J* = 6.2 Hz, 2H), 8.47 (m, 2H), 8.31 (d, *J* = 8.0 Hz, 2H), 8.19 (d, *J* = 1.4 Hz, 1H), 8.14 (m, 2H), 7.94 (d, *J* = 5.3 Hz, 1H), 7.76 (m, 2H), 7.68 (m, 2H), 7.52 (m, 2H). Anal. Calcd for $C_{55}H_{31}N_{13}O_2Ru\cdot(PF_6)_2$: C 55.24, H 2.61, N 15.23; Found: C 55.49, H 2.84, N 15.39. ESI-MS (positive ion): m/z 503.59 $[M]^{2+}$; 1006.17 $[M-PF_6]^+$.

Complex **2**: Mass (Yield): 0.124 g (50.3%). ^{1}H NMR (CD_3CN, δ ppm): 9.61 (d, *J* = 8.3 Hz, 2H), 9.55 (d, *J* = 8.1 Hz, 2H), 9.09 (d, *J* = 6.1 Hz, 2H), 9.00 (d, 1H), 8.45 (dd, *J* = 6.7, 3.6 Hz, 2H), 8.33 (m, 2H), 8.21 (d, *J* = 5.4 Hz, 1H), 8.14 (m, 2H), 8.00 (m, 1H), 7.79 (m, 4H), 7.59 (t, *J* = 6.8 Hz, 1H). Anal. Calcd for $C_{55}H_{31}N_{13}O_2Ru\cdot(PF_6)_2$: C 55.24, H 2.61, N 15.23; Found: C 55.14, H 2.98, N 15.25. ESI-MS (positive ion): m/z 503.59 $[M]^{2+}$; 1006.17 $[M-PF_6]^+$.

Complex **3**: Mass (Yield): 0.128 g (51.9%). ^{1}H NMR (CD_3CN, δ ppm): 9.71 (d, *J* = 8.2 Hz, 2H), 9.65 (t, *J* = 5.6 Hz, 2H), 9.07 (d, *J* = 6.2 Hz, 2H), 8.62 (d, *J* = 7.0 Hz, 1H), 8.49 (m, 1H), 8.32 (m, 1H), 8.21 (d, *J* = 8.1 Hz, 1H), 8.15 (dd, *J* = 7.7, 3.4 Hz, 2H), 8.00 (d, *J* = 8.6 Hz, 2H), 7.82 (m, 4H), 7.60 (dd, *J* = 8.3, 3.2 Hz, 2H). Anal. Calcd for $C_{55}H_{31}N_{13}O_2Ru\cdot(PF_6)_2$: C 55.24, H 2.61, N 15.23; Found: C 55.41, H 2.59, N 14.87. ESI-MS (positive ion): m/z 503.59 $[M]^{2+}$; 1006.17 $[M-PF_6]^+$.

DNA binding

Calf thymus DNA (CT-DNA, Sigma) was dissolved in NaCl (25 mM) and Tris (5 mM, pH 7.0). Concentrations were determined spectrophotometrically (ε260 = 6600 M^{-1} cm^{-1}). DNA purity was verified (A260/A280 > 1.9). UV-Vis titrations and intrinsic binding constants were performed following the methods described by Liu et al.[45] Viscosity experiments were performed as described by Gill et al.[46] EB titration was conducted by monitoring the decrease in fluorescence intensity of the EB-DNA system (λ_{ex} = 520 nm, λ_{em} = 595 nm) upon incremental addition of the Ru(II) complexes, following the procedure described by Chauhan et al.[47] and Lakowicz et al.[48]

Molecular docking

The established DNA structure from the protein data bank (PDB ID: 1BNA) was taken as the initial structure for subsequent molecular docking. The initial structure was prepared with the prepare_receptor4 script in MGLTools 1.4.2, and Gasteiger partial charges were assigned. For the ruthenium complex, Gasteiger partial charges were assigned using the prepare_ligand4 script in MGLTools 1.4.2. Molecular docking experiments were performed using AutoDock Vina v1.2.5, with the docking centre set at the centroid of the DNA. The grid box was defined as a cube with 40 Å side length. A total of 20 conformations were generated, which were ranked according to docking scores, and the top-ranked conformation (Rank 1) was selected for further analysis.

Cell lines and culture conditions

MCF7 breast cancer, A549 lung cancer, HeLa cervical cancer and MRC5 normal lung fibroblast cells were cultured in DMEM supplemented with 10% FBS and 1% penicillin/streptomycin at 37 °C in 5% CO_2. Cells were subcultured at 80-90% confluency using trypsin and verified to be mycoplasma-free. Treatments were applied 24 h post-seeding unless otherwise noted.

Cellular uptake and microscopy

Cells were seeded onto confocal-compatible dishes and incubated for 24 h. They were then treated with the indicated complexes as described in the main text. After washing with PBS, cells were fixed with 4% paraformaldehyde (PFA) for 15 min at room temperature (RT), followed by an additional PBS wash. Nuclei were counterstained with DAPI (5 µg/mL, 15-20 min, 37 °C). Where indicated, plasma membranes were stained with CellMask dye prior to fixation for co-localisation analysis. Confocal imaging was performed using a Zeiss LSM 980 laser scanning microscope. Complexes **1**-**3** were excited at 488 nm, and their metal-to-ligand charge transfer (MLCT) emission was collected at 600-750 nm. Image processing and quantification were performed using the Zeiss LSM Image Browser or ImageJ. For each condition, at least 200 nuclei were analysed.

Singlet oxygen detection (SOSG)

Singlet oxygen generation was assessed using SOSG probe. SOSG (5 µM) was prepared in PBS and mixed with complexes **1**-**3** (10 µM). Fluorescence was recorded on a microplate reader at

λ_{ex} = 504 nm and λ_{em} = 525 nm at 0-30 min. Background fluorescence from SOSG-only and buffer-only controls was subtracted. A singlet oxygen-generating control (rose bengal, 10 µM) was included under identical conditions with white-light irradiation to confirm probe responsiveness.

MTT assay

MCF7, A549, HeLa, and MRC5 cells were seeded in 96-well plates at a density of 5×10^3 cells per well and treated as described in the main text. After treatment, the medium was removed and replaced with MTT reagent (thiazolyl blue tetrazolium bromide, 0.5 mg/mL). Plates were incubated for 3 h, after which the resulting purple formazan crystals were dissolved in 100 µL DMSO. Absorbance was measured at 570 nm (reference wavelength 620 nm) using a Tecan Infinite F50 microplate reader. The half-maximal inhibitory concentration (IC_{50}) values were determined from dose-response curves using GraphPad Prism software.

Drug interaction analysis

Dose-effect curves for individual and combination treatments were generated from MTT assay data. Combination index (CI) values were calculated using CalcuSyn and CompuSyn software (Biosoft, Cambridge, UK) following the Chou-Talalay method.[49, 50] CI < 0.9 indicates synergism, CI = 0.9-1.0 denotes additivity, and CI > 1.0 suggests antagonism. GraphPad Prism software was used to visualize CI values on a three-color scale, where blue, white, and red represent synergistic, additive, and antagonistic interactions, respectively.

Clonogenic survival assay

MCF7, A549, and HeLa cells were seeded in 6-well plates at 1×10^3 cells per well and treated as described in the main text. After treatment, the medium was replaced with drug-free culture medium and cells were allowed to form colonies for 7-14 days. Colonies were fixed with cold methanol (100%, 20 min, 4 °C), stained with 0.5% crystal violet for 20 min, and rinsed with water. Colony images were captured using a digital camera, and colonies were quantified using ImageJ. The surviving fraction was calculated relative to untreated controls.

Cell cycle analysis

MCF7, A549, and HeLa cells were seeded in 6-well plates at 1×10^5 cells per well and treated as described in the main text. After treatment, cells were trypsinized, washed twice with PBS, and fixed in ice-cold 70% ethanol overnight at 4 °C. Fixed cells were washed twice with PBS, resuspended in PBS containing RNase A (100 μg/mL), and incubated for 15 min. Cells were stained with propidium iodide (PI, 20 μg/mL) for 30 min at 37 °C in the dark. Flow cytometric analysis was performed using a NovoCyte flow cytometer (Agilent Technologies, USA) and NovoExpress software, acquiring at least 10,000 events per sample.

Apoptosis Annexin V-FITC/PI assay

MCF7, A549, and HeLa cells (1×10^5 cells/well) were seeded in 6-well plates and treated as described in the main text. After treatment, cells were harvested, washed twice with PBS, and resuspended in 500 μL binding buffer containing 5 μL Annexin V-FITC (Elabscience). Following incubation for 20 min at room temperature, 5 μL PI (20 μg/mL) was added immediately before analysis by flow cytometry. Data were analyzed using NovoExpress software, with at least 10,000 cells recorded per sample.

Immunoblotting

MCF7 cells (1×10^6 cells/dish) were seeded in 60 mm dishes, allowed to adhere for 24 h, and treated as described in the main text. After treatment, cells were lysed in RIPA buffer supplemented with protease and phosphatase inhibitors. Protein lysates (40 μg) were separated on 4-20% Mini-PROTEAN TGX SDS-PAGE gels (Beyotime) and transferred to methanol-activated PVDF membranes. Membranes were blocked for 1 h at room temperature in 5% BSA or skimmed milk (in TBS-T: 0.1% Tween-20 in TBS), then incubated overnight at 4 °C with primary antibodies: p-ATM (Ser1981, 1:500), ATM (1:1000), p-H2AX (Ser139, 1:1000), cleaved caspase-3 (1:1000), GAPDH (1:10000), and β-actin (1:1000). After washing, membranes were probed with HRP-conjugated secondary antibodies (1:10000, 1 h, RT). Protein bands were visualized using Immobilon Western Chemiluminescent HRP substrate (Sigma-Aldrich) and a ChemiDoc™ MP Imaging System. Densitometry was performed with ImageJ, and GAPDH or β-actin served as loading controls.

Immunofluorescence

Cells were seeded in confocal-compatible culture dishes and treated as described in the main text. After washing with PBS, cells were fixed with 4% PFA for 15 min at room temperature, permeabilized with 0.5% Triton X-100 for 15 min on ice, and washed with PBS. Samples were blocked with 3% BSA in PBS-T (PBS + 0.1% Tween 20) for 1 h, followed by incubation with anti-γH2AX (Ser139) antibody (1:100 in 3% BSA/PBS-T) overnight at 4 °C. After washing, cells were incubated with Alexa Fluor 488-conjugated secondary antibody (1:200) for 1 h at room temperature in the dark and counterstained with DAPI (5 μg/mL, 30 min). Fluorescence images were acquired using a confocal microscope and analysed with ImageJ. A minimum of 200 nuclei were analysed per condition.

Determination of ROS levels

MCF7 cells were seeded in 6-well plates at 1×10^5 cells per well and allowed to adhere for 24 h. Cells were treated as described in the main text, with or without 5 mM N-acetylcysteine (NAC). After incubation, cells were washed with PBS and stained with 10 μM DCFH-DA in serum-free medium for 60 min at 37 °C in the dark. Cells were then washed three times with serum-free medium, and DCF fluorescence was imaged using a fluorescence microscope. ImageJ software was used to quantify ROS levels.

Statistical analysis

Data are presented as mean ± SD. All experiments were performed in triplicate and repeated at least three times. Statistical significance was assessed using one-way ANOVA and Student's *t*-test ($P < 0.05$) in GraphPad Prism 9.

Results and discussion

Physicochemical characterization of Ru(II) polypyridyl complexes

We synthesized a series of nitro-substituted ruthenium(II) polypyridyl complexes of the general formula $[Ru(dppz)_2(NPIP)]^{2+}$, where NPIP = 2-(nitrophenyl)imidazo[4,5-*f*][1,10]phenanthroline and the nitro group was introduced at the ortho (**1**), meta (**2**), or para (**3**) position of the pendant phenyl ring (Fig. 1a). Although employing enantiomerically pure Δ and Λ forms would be preferable, compounds **1**-**3** were prepared as racemic mixtures, as is customary in early-stage biological evaluation of octahedral Ru(II) polypyridyl complexes.

Complex identity and formulation were confirmed by complementary spectroscopic data (Fig. S1-S7). FT-IR spectra exhibited characteristic nitro stretching bands ($\nu_{as}(NO_2)$ ~1500-1530 cm^{-1}, and $\nu_s(NO_2)$ ~ 1340-1360 cm^{-1}) together with the expected polypyridyl aromatic vibrational envelope, consistent with retention of the nitro substituent upon coordination. Positive-ion ESI-MS spectra showed dominant signals at m/z 503.59 corresponding to the doubly charged complex cation, together with peaks at m/z 1006.17 attributable to the singly charged $[M\text{-}PF_6]^+$ species, supporting the proposed dicationic formulation. ^1H NMR spectra (with COSY assignments provided in the Supporting Information) were consistent with the expected Ru-polypyridyl framework and enabled differentiation of the regioisomeric NPIP ligands through diagnostic coupling patterns within the nitrophenyl region. Collectively, these data confirm preservation of the coordinated nitro functionality and integrity of the $[Ru(dppz)_2(NPIP)]^{2+}$ scaffold. Positional isomerism of the nitro substituent (ortho, meta, para) thus provides a means to modulate ligand electronics and steric environment without perturbing the overall coordination geometry.

The complexes exhibited characteristic MLCT absorption bands in the visible region (Fig. 1b) and red-region phosphorescence emission in acetonitrile upon MLCT excitation at 460 nm (Fig. 1c). Lifetime measurements in acetonitrile showed that complexes **1-3** shared closely similar biexponential ^{3}MLCT decay profiles, with τ_1 values of 160-191 ns and τ_2 values of 519-614 ns, confirming that nitro substitution exerts little influence on their excited-state photophysical behaviour (Fig. S8, Table S1). Octanol-water partition coefficients (log P) indicated moderate lipophilicity, with values of 0.53 (**1**), 0.23 (**2**), and 0.46 (**3**) (Fig. 1d). As the parent complex has a log P value of 0.42,[43] this indicates that hydrophobicity is decreased for substitution of a nitro group at the *meta*-position; However, the opposite is seen for substitution at the *ortho*- and *para*-positions where instead a slight increase in hydrophobicity is apparent.

Viscosity measurements with calf-thymus DNA (CT-DNA) confirmed that each complex intercalated DNA (Fig. 1e) while binding studies revealed high binding affinities, with binding constants (K_b) of 8.6×10^6 M^{-1} (**1**), 1.0×10^6 M^{-1} (**2**), and 2.5×10^6 M^{-1} (**3**) (Fig. 1f, Table S2), comparable to results previously reported for Ru-PIP ($K_b = 2.5 \times 10^6$ M^{-1}).[43] Together, these photophysical and DNA-binding properties indicate that the Ru-dppz core remains electronically intact across the series, where close inspection between Ru-PIP and **1**-**3** shows

that nitro substitution is able to fine-tune both hydrophobicity and DNA binding affinity in a position-dependent fashion.

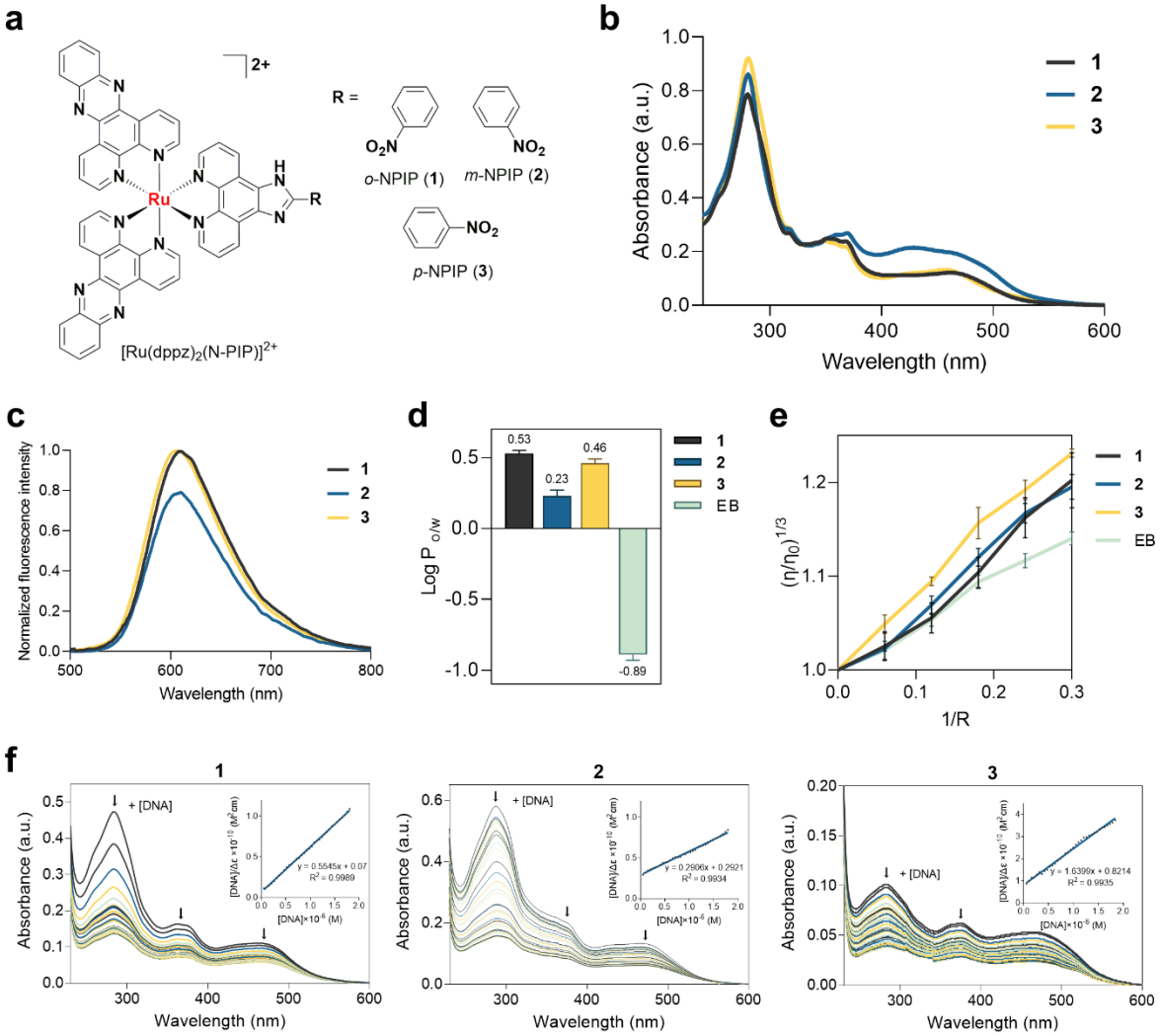

Fig. 1: Physicochemical characterization of Ru(II) polypyridyl complexes. a) Chemical structures of Ru(II) complexes $[Ru(dppz)_2(N\text{-}PIP)]^{2+}$ (**1**-**3**), differing by the position of the nitro substituent on the pendant benzene ring. b) UV-visible absorption spectra of complexes **1**-**3** (20 µM) in TBS containing 1% DMSO. c) Fluorescence emission spectra of complexes **1**-**3** (100 µM) in acetonitrile (λ_{ex} = 460 nm). d) Partition coefficients (log P) of complexes **1**-**3** measured in octanol/water. Data represent mean ± SD from three independent experiments. e) Viscosity measurements of complexes **1**-**3**. Data represent mean ± SD from three independent experiments. f) DNA-binding profiles of complexes **1**-**3**.

Molecular docking studies with canonical B-DNA (PDB ID: 1BNA) revealed that the planar dppz moiety intercalates between base pairs, while the nitro-substituted NPIP ligand contributes stabilizing electrostatic interactions (Fig. 2a-c). As shown in Figure 2b, complex **3**

engages in π-π stacking with DC-21 and DC-3, complemented by additional electrostatic contacts with DC-3 and DA-18. The calculated binding free energy (-11.16 kcal/mol) indicates strong affinity, consistent with classical DNA intercalation rather than groove binding. This intercalative binding mode was further supported by ethidium bromide displacement assays. Progressive quenching of EB-DNA fluorescence upon addition of the Ru(II) complexes afforded Stern-Volmer constants (K_{sv}) of 1.5×10^4-2.3×10^4 M^{-1}, signifying strong competitive displacement of EB and confirming efficient intercalation between DNA base pairs through π–π stacking interactions (Fig. 2d, Table S3).

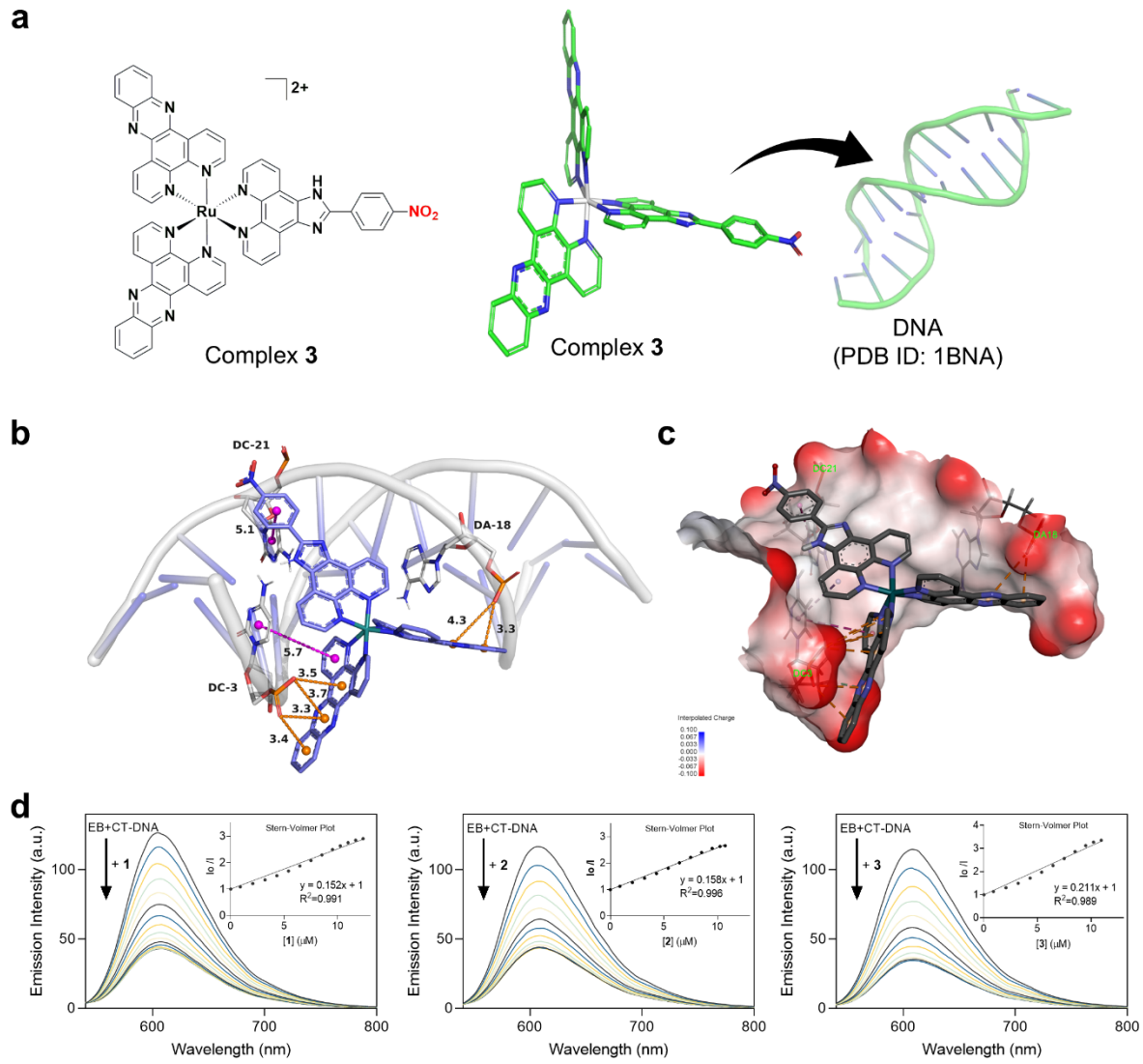

Fig. 2: Molecular docking of 3 to DNA. a) Structure of **3**. b) Structure of DNA (PDB ID: 1BNA) c) Interaction diagram of DNA and **3**: white cartoon/sticks represent DNA, purple sticks represent **3**, pink dashed lines indicate π–π interactions, and orange dashed lines indicate electrostatic interactions. d) Fluorescence quenching titration spectra of EB/CT-DNA

([DNA]/[EB] = 4.3-4.9) upon successive addition of **1** (12.8 µM), **2** (11.9 µM), **3** (11.4 µM) in Tris buffer (5 mM, pH = 7.2) at 25 °C, with excitation at λ_{max} = 520 nm. Inset: Stern-Volmer plot of EB-DNA fluorescence quenching by ruthenium complexes under the same condition. Data were fitted to the Stern-Volmer equation $I_0/I = 1+K_{SV}[Q]$ to determine the quenching constant K_{SV}.

Cellular uptake and subcellular distribution of Ru(II) complexes

Cellular uptake was assessed in MCF7 and HeLa cells using confocal microscopy. All complexes were internalized within 1 h, but no detectable nuclear emission was observed under the imaging conditions used (Fig. 3a and Fig. S9). Complexes **2** and **3** exhibited pronounced colocalisation with the plasma membrane, as shown by overlap with CellMask Deep Red staining (Fig. 3b,c). DAPI counterstaining further indicated minimal nuclear-associated signal, suggesting that, under these conditions, the complexes preferentially associate with cellular membranes rather than translocate to the nucleus. Collectively, these results demonstrate that Ru(II) complexes **1**-**3** are lipophilic DNA intercalators with micromolar-to-submicromolar binding affinities, while differing from classical nuclear-targeted Ru-dppz probes by exhibiting distinct plasma membrane-associated localisation, particularly for the *meta*- and *para*-nitro derivatives. These observations indicate that positional isomerism of the nitro substituent (*ortho, meta, para*) influences not only steric and electronic effects on DNA binding, but also intracellular distribution. Although no detectable nuclear emission was observed by confocal microscopy, DNA intercalation remains relevant at the molecular level. It is also important to note that the absence of nuclear emission does not necessarily indicate a lack of nuclear uptake, as redox-mediated quenching and/or aggregation can attenuate luminescence in cells.

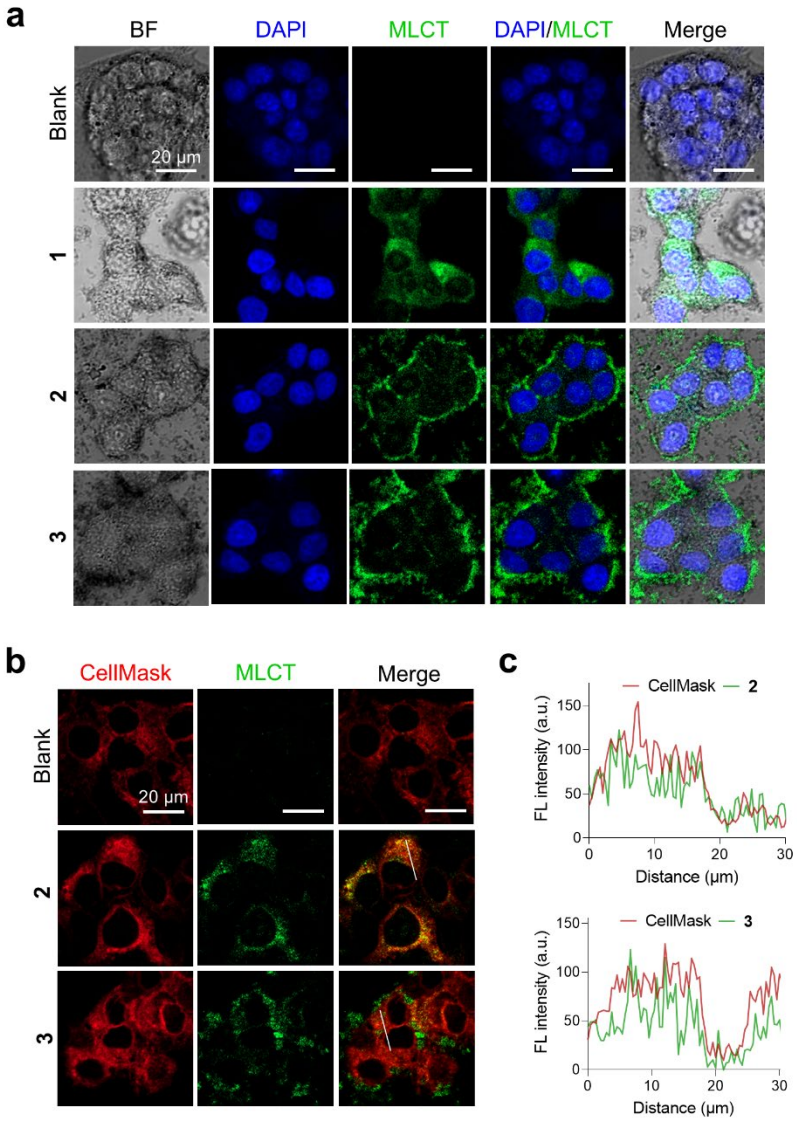

Fig. 3: Cellular uptake and subcellular distribution of Ru(II) complexes in cancer cells. a) Confocal fluorescence images of MCF7 cells treated with complexes **1**-**3** (100 µM, 1 h). b) Colocalisation of complexes **2** and **3** with the plasma membrane marker CellMask Deep Red in MCF7 cells. c) Colocalisation profile from b. Complexes were excited at 488 nm, and emission was collected between 600-750 nm. Nuclei were counterstained with DAPI. Scale bars = 20 µm.

Cytotoxicity and DNA damage induced by Ru(II) complexes

Cytotoxicity of complexes **1**-**3** was evaluated in cancer (MCF7, A549, HeLa) and non-cancerous (MRC5) cell lines following 72 h exposure. The complexes exhibited comparable activity across cancer cells, with IC_{50} values in the range of 37-44 µM, while all were markedly less toxic toward MRC5 cells (IC_{50} > 100 µM) (Fig. 4a and Table S4). Despite limited nuclear accumulation, DNA damage was apparent, where immunofluorescence in MCF7 cells

revealed a marked increase in γH2AX foci, with mean foci counts increasing from ~1 per nucleus in untreated controls to 9-20 across complexes **1**-**3** (Fig. 4b). Western blotting confirmed dose-dependent DNA damage signalling, with pATM/ATM ratios increased up to ~3.7-fold and γH2AX up to ~2.4-fold relative to untreated controls following treatment (Fig. 4c).

The low nuclear uptake of **1**-**3**, observed by confocal microscopy, prompted investigation of intracellular ROS generation as an alternative principal pathway for DNA damage.[51] Accordingly, ROS levels were quantified in MCF7 cells using the DCF dye. This showed that complexes **1**-**3** induced a > 20-fold increase in ROS after 24 h, which was strongly attenuated by co-incubation with the antioxidant N-acetylcysteine (NAC) (28.8 ± 2.7 for **3** alone vs. 2.4 ± 0.7 for **3** with NAC; Fig. 4d).

Altogether, complexes **1**-**3** induce DNA damage through both replication stress signalling and oxidative stress, providing a mechanistic basis for their selective cytotoxicity in cancer cells while sparing non-malignant fibroblasts. ATM pathway activation and generation of γH2AX foci provides clear evidence that DNA double-strand break damage is induced by **1**-**3**. It is interesting to compare these results to our previous work which established that Ru-PIP intercalates into DNA and activates DDR signalling *without* inducing DSBs or apoptosis,[43] highlighting how subtle ligand modifications can profoundly alter biological behaviour. Consistent with the subcellular distribution observed for **1**-**3**, it is likely that DNA damage is induced indirectly by the high intracellular levels of ROS generated by treatment. To further evaluate ROS identity, we assessed singlet oxygen ($^1O_2$) generation using SOSG under the same dark conditions employed in the biological experiments. No increase in SOSG fluorescence was observed relative to probe-only controls, indicating that detectable $^1O_2$ is not produced under these conditions (Fig. S10). These findings suggest that the oxidative stress observed is unlikely to be dominated by a singlet-oxygen pathway and more likely reflects non-$^1O_2$ ROS species arising from redox or bioreductive processes. Previous studies have shown that ruthenium complexes capable of inducing oxidative stress can trigger apoptosis, mitochondrial dysfunction, cytoskeletal disruption, and DNA damage through ROS-mediated pathways.[52] Similar pro-oxidant and pro-apoptotic responses have been reported for Ru systems targeting lung and melanoma cancer cells, supporting a general role for redox imbalance in their anticancer activity.[53]

Although phototoxic RPCs commonly generate ROS upon exposure to light,[54] complexes **1**-**3** were shielded from light over the course of our studies so a similar mechanism of ROS generation seems unlikely. However, nitroaromatic moieties are bioreductively active under hypoxic conditions, generating reactive intermediates such as nitroso or hydroxylamine species which induce oxidative stress or form covalent DNA/protein adducts. These pathways are well documented in classical hypoxia-activated prodrugs, including tirapazamine,[55, 56] and nitroimidazole-based agents.[57-59] Consistent with this, Fernandez et al. reported that nitro substitution enhanced the anticancer activity of metal-organic chains.[60] Such mechanisms could potentially contribute to the ROS-mediated enhancement of DSB observed with complex **3**.

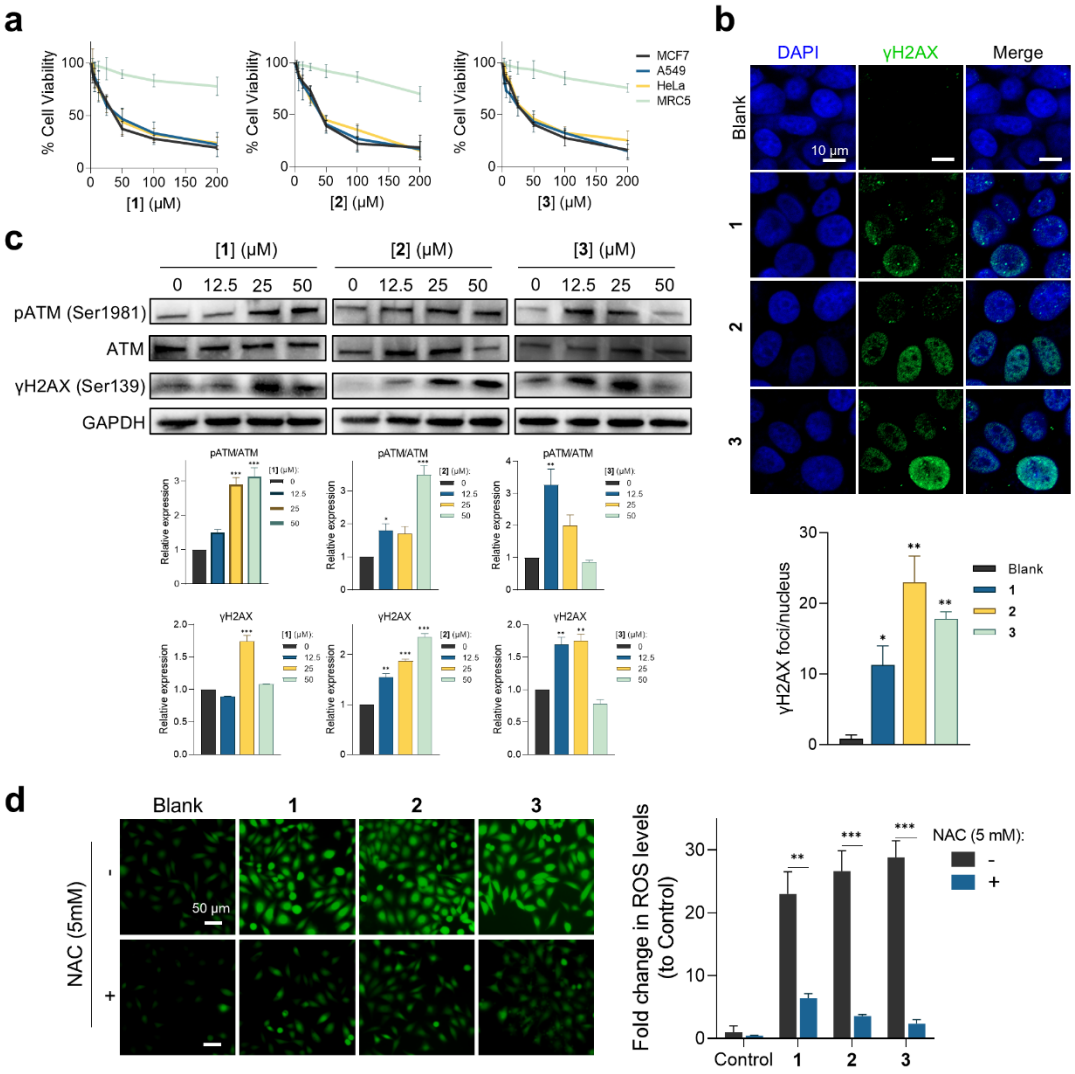

Fig. 4: Cytotoxicity and DNA damage induced by Ru(II) complexes. a) Cell viability of MCF7 (breast cancer), A549 (lung cancer), HeLa (cervical cancer) and MRC5 (normal lung) cells after treatment with complexes **1**-**3** for 72 h, as determined by MTT assay. Data represent mean ± SD from three independent experiments. b) Top, immunofluorescence analysis of γH2AX foci (green) in MCF7 cells treated with complexes **1**-**3** (25 μM, 3 h). Nuclei were counterstained with DAPI. Bottom, quantification of γH2AX foci per nucleus. Data are mean ± SD from two independent experiments; at least 200 nuclei were counted per group. Scale bars = 10 μm. c) Top, western blot analysis of whole-cell lysates from MCF7 cells treated with complexes **1**-**3** (0, 12.5, 25 μM, 3 h), probed for DNA damage markers γH2AX and pATM. Bottom, relative protein expression normalized to GAPDH. Data are mean ± SD from two independent experiments. **P* < 0.05, ***P* < 0.01 and ****P* < 0.001 by ANOVA. Uncropped blots are in Fig S1. d) Intracellular reactive oxygen species (ROS) levels measured using 2',7'-dichlorofluorescein (DCF) fluorescence in MCF7 cells following the indicated treatments for 24 h. ROS-positive cells indicated by DCF (green). Scale bars = 50 μm. Data expressed as mean ± SD of three independent experiments. **P* < 0.05, ***P* < 0.01 and ****P* < 0.001 by student *t*-test.

Synergistic activity of Ru(II) complex 3 with ATR inhibitors

Our earlier findings established that complexes **1**-**3** strongly bind DNA (Fig. 1f), induce DSBs as evidenced by γH2AX and pATM activation (Fig. 4b,c), and elevate ROS levels (Fig. 4d). Notably, despite minimal nuclear accumulation (Fig. 3a-c), complex **3** was able to trigger pronounced genotoxic stress through combined intercalative and ROS-mediated mechanisms. Given that ATR signalling is a critical survival pathway under replication stress, we hypothesized that pharmacological ATR inhibition would enhance the cytotoxicity of these Ru(II) complexes. To test this, complex **3** was evaluated in combination with the clinically relevant ATR inhibitors berzosertib (VE-822, IC_{50}: ATR = 19 nM) and ceralasertib (AZD6738, IC_{50}: ATR = 74 nM).[61]

Combination treatment resulted in substantial potentiation of cytotoxicity in cancer cell lines, whereas MRC5 fibroblasts remained largely resistant (Fig. 5a and Fig. S12). Synergy was confirmed by combination index (CI) analysis using the Chou-Talalay method (Fig. 5b and Fig. S13). In MCF7 cells, co-treatment with berzosertib (0.01 μM) and complex **3** showed CI values of 0.61 (12.5 μM), 0.50 (25 μM), and 0.31 (100 μM), indicating strong synergy across a broad concentration range. Even at higher berzosertib levels (0.1 μM), synergy persisted (CI = 0.86 at 25 μM complex **3**). Ceralasertib combinations exhibited similar trends, with CI values as low as 0.54 (100 μM complex **3** at 0.01 μM ATRi). Comparable synergistic effects were observed in A549 and HeLa cells, where in A549, berzosertib with complex **3** showed CI = 0.59 (25 μM complex **3** at 0.01 μM ATRi), whereas in HeLa cells, synergy was particularly pronounced, with ceralasertib (0.1 μM) yielded CI of 0.18 at 200 μM complex **3**.

To assess long-term proliferative capacity, clonogenic survival was examined following 72 h drug exposure. While single-agent treatments modestly reduced colony formation, co-treatment profoundly inhibited clonogenic survival in MCF7, A549, and HeLa cells (Fig. 5c). For example, in MCF7 cells, complex **3** alone reduced viability to ~73-75%, whereas ATRi alone showed viability at ~82-86%. Strikingly, the combination decreased survival to ~7-10%. A similar trend was observed in A549 cells, where monotherapy treatments maintained ~67-87% viability, but dual treatment reduced survival to ~ 8-16%. In HeLa cells, viability decreased from ~68-79% with single agents to ~12-18% with the combination. Additionally, treatment with ATRi in a concentration gradient, both with or without compound **3**,

demonstrated that **3** sensitizes cells to ATRi, further confirming their synergy (Fig. 5d and Fig. S14).

Flow-cytometric analysis of MCF7 cells showed that complex **3** or berzosertib alone caused only modest phase changes, with complex **3** slightly increasing S-phase (~15% to ~21%) and G_2/M, and berzosertib producing a mild G_1 decrease. In contrast, the combination induced a marked rise in sub-G_1 (~22%) with reductions in G_1 and S-phase, whereas G_2/M did not increase further, consistent with apoptosis rather than checkpoint arrest (Fig. 5e). Similar trends were observed in A549 and HeLa cells (Fig. S15).

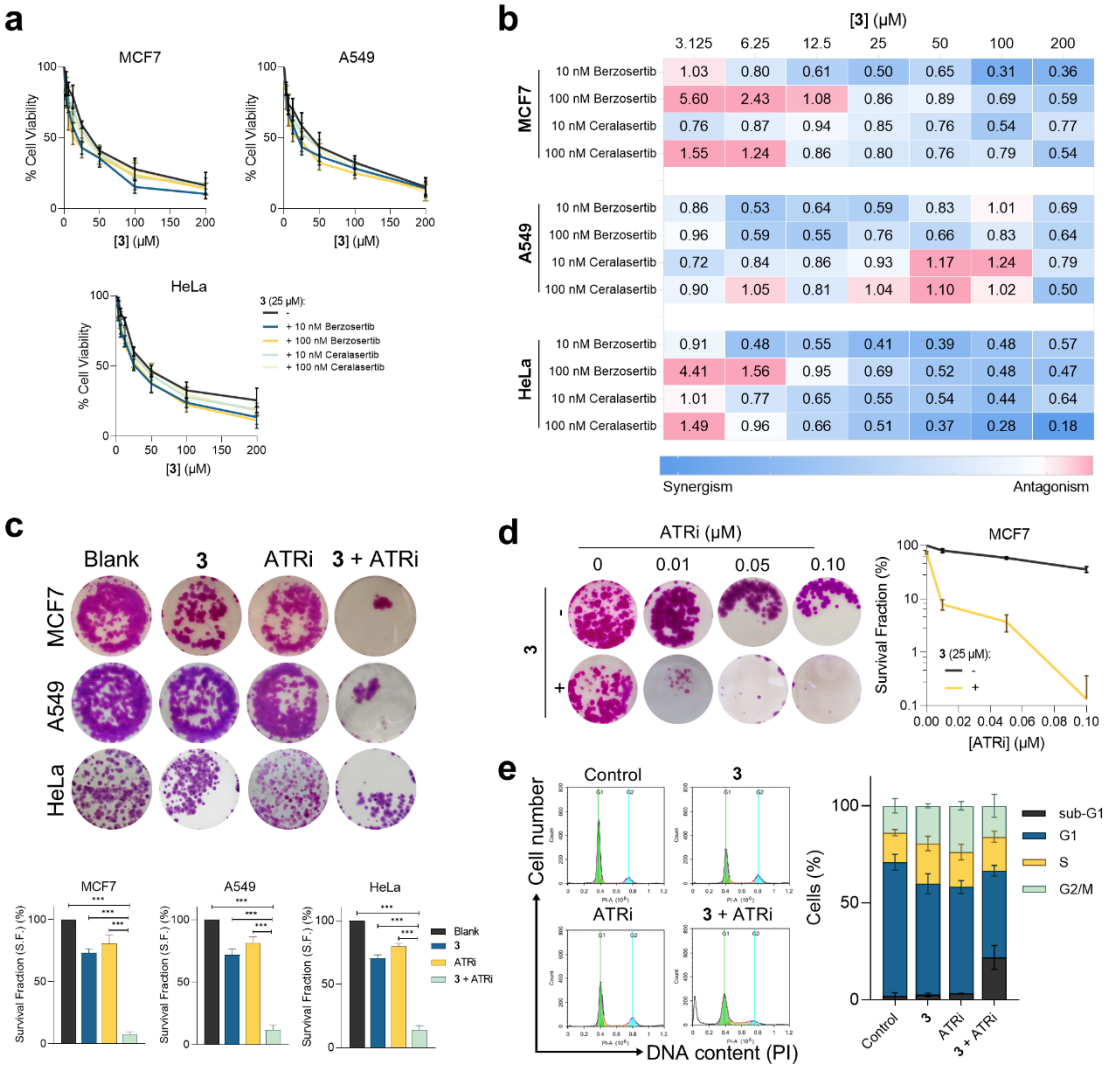

Fig. 5: Synergistic activity of Ru(II) complex 3 with ATR inhibitors. a) Cell viability of MCF7, A549 and HeLa cells treated with complex **3** in combination with ceralasertib (0.01 μM) or berzosertib (0.01 μM) for 72 h, assessed by MTT assay. Data represent mean ± SD from three independent experiments. b) Combination indices calculated using the Chou-Talalay method. CI < 1 = synergism and CI >1 antagonism. c) Clonogenic survival of cells treated for 72 h with

complex **3** (25 μM) in combination with berzosertib (0.01 μM). d) Clonogenic survival of MCF7 cells after treated with concentration gradient of ATRi in the presence and absence of **3** (25 μM). e) Cell-cycle distribution of MCF7 cells treated for 72 h with complex **3** (25 μM) in combination with berzosertib (0.01 μM). Data represent mean ± SD from three independent experiments. ***$P < 0.001$ by ANOVA.

Mechanistic basis of synergistic activity between complex 3 and ATR inhibition

To assess the mechanistic basis of the observed synergy, we examined DNA damage and apoptosis following combined treatment with complex **3** and ATR inhibition. Immunofluorescence staining for γH2AX revealed a sharp increase in DNA damage foci in MCF7 cells exposed to the combination treatment, compared with either agent alone (Fig. 6a). Quantification data showed that while complex **3** or ATR inhibition alone induced ~15-18 γH2AX foci per nucleus, the combination elevated this to ~24-26 foci per nucleus, representing a >1.5-fold enhancement relative to single agents. Consistent with enhanced DNA damage, flow cytometric Annexin V-FITC/PI analysis demonstrated that apoptotic cell death increased from ~12-14% with single-agent treatment to ~36-39% under combination conditions (Fig. 6b and Fig. S16). Western blotting further confirmed these findings in which γH2AX levels significantly increased by ~2-fold relative to untreated cells, and cleaved caspase-3 accumulated to ~3.6-3.9-fold above baseline under dual treatment, surpassing either monotherapy (Fig. 6c).

In addition to this, we tested the parent complex Ru-PIP for synergy with ATRi Berzosertib or Ceralasertib and found a similar level of synergy as for complex **3** (Fig. S17). A similar mechanism for synergy was present, where elevated DNA damage and accompanying apoptosis in cells treated with Ru-PIP combined with ATRi Berzosertib or Ceralasertib compared to single-agent conditions was found (Fig. S18). These results additionally confirm previous findings that Ru-PIP does not generate elevated levels of DSB damage in the form of γH2AX expression or foci (Fig. S18), contrasting with the behaviour of **3**. This observation is consistent with nitro-substitution of the Ru-PIP scaffold facilitating an altered DNA damage response, specifically facilitating DSB generation. However, these results also indicate that this is not a requirement for synergy with ATRi, as Ru-PIP is equally proficient in this capacity.

Combining ATR inhibitors with DNA-damaging agents represents a promising anticancer strategy that exploits synthetic lethality, wherein the combined treatment is far more effective than either agent alone. In this study, complex **3** and the parent molecule Ru-PIP both exhibit strong synergism with ATR inhibitors across multiple cancer cell lines. Mechanistically, complex **3** intercalates into DNA and generates ROS, elevating replication stress and triggering DDR signalling. ATR inhibition concurrently suppresses the primary checkpoint response, preventing repair of DNA single-strand breaks or stalled replication forks and leading to catastrophic DNA damage and apoptotic cell death. Importantly, this combination selectively targets cancer cells over normal fibroblast cells, reflecting selective vulnerability of malignancies with heightened replication stress dependencies. This approach has shown significant synergy with DDR-targeted therapies in other studies, including ionizing radiation,[62] PARP inhibitors,[39-42] and gemcitabine.[63] Interestingly, a large-scale combination screen highlights strong synergy between ATRi and agents targeting DNA topoisomerases, PLK1, ribonucleotide reductase, PARP, and checkpoint proteins.[64] Sequential ATR and PARP inhibition has further been shown to overcome resistance to DNA-damaging agents,[65] highlighting the broader potential of combinatorial DDR-targeted strategies.

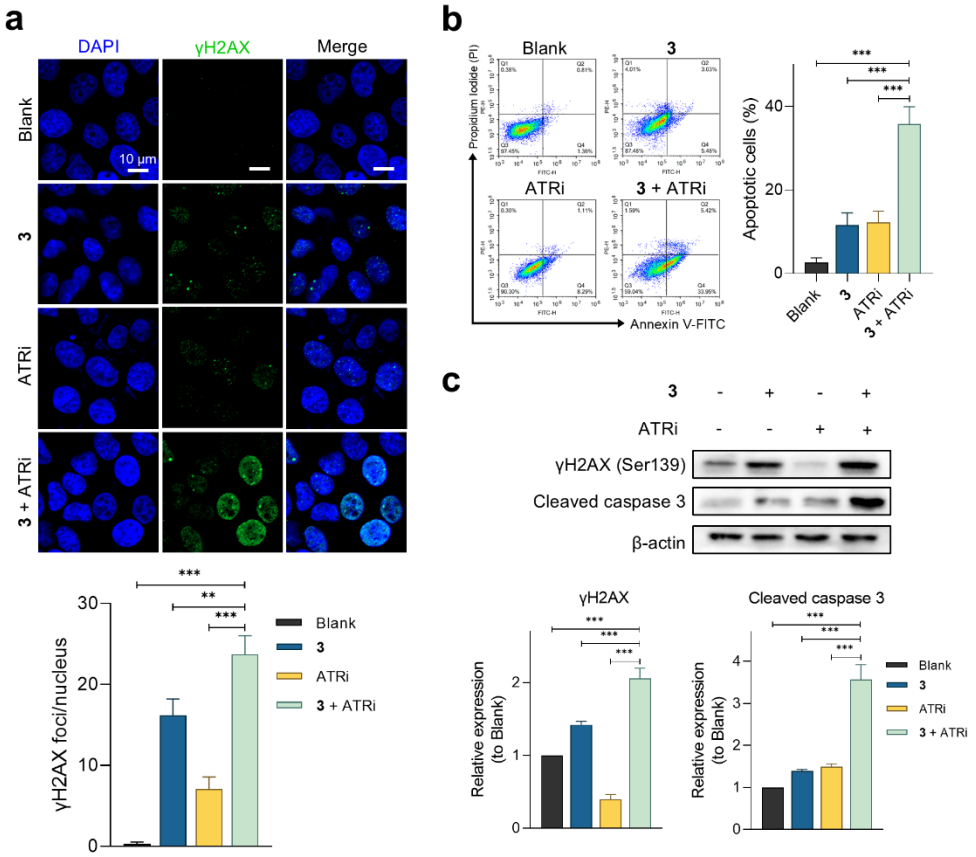

561 **Fig. 6: Mechanistic basis of synergistic activity between complex 3 and ATR inhibition.** a)
562 Immunofluorescence detection of γH2AX foci (green) in MCF7 cells treated with complex **3**
563 (25 μM), berzosertib (0.01 μM), or the combination for 24 h. Nuclei were counterstained with
564 DAPI (blue). Quantification of γH2AX foci per nucleus is shown (mean ± SD, ≥ 200 nuclei per
565 condition, two independent experiments). Scale bars, 10 μm. b) Apoptotic cell death assessed
566 by Annexin V-FITC/PI flow cytometry under the same treatment conditions. 72 h treatment.
567 (mean ± SD, three independent experiments). c) Western blot analysis of DNA damage
568 (γH2AX) and apoptosis (cleaved caspase 3), with β-actin as a loading control (24 h treatment)
569 Representative blots and quantification are shown (mean ± SD, two independent
570 experiments). Uncropped blots are in Fig S19. **P* < 0.05, ***P* < 0.01 and ****P* < 0.001 by
571 ANOVA.
572

573 **Conclusions**

574 In this study, positional nitro substitution of the Ru-PIP scaffold offers a means to fine-tune
575 DNA-binding behaviour and the resulting DNA damage response, shifting the cellular
576 response toward replication stress and ROS-associated DNA damage. The strong synergy
577 observed between the *para*-nitro derivative and ATR inhibitors, together with comparable
578 synergy retained by the parent complex Ru-PIP, demonstrates that chemically induced
579 replication stress can be effectively exploited through checkpoint inhibition. These findings

provide a clear mechanistic rationale for combining metal-based DNA-intercalating agents with DDR-targeted therapies and establish guiding principles for the rational design of next-generation ruthenium-based anticancer agents.

Author contributions

HA and MG conceived and designed the project. GYC and NAY conducted the experiments, handled data curation, data analysis, data interpretation, and prepared the figures. Resources and supervision were provided by HA, MG, XT and SLC. HA, MG and NAY acquired the fundings. GYC and NAY wrote the original draft of the manuscript. All authors revised and approved the final version of the manuscript.

Conflict of interest

The authors declare no conflict of interest.

Data availability

The data supporting this article have been included as part of the supplementary information (SI). Supplementary information is available.

Acknowledgements

This work was supported by grants from the Universiti Putra Malaysia through Geran Putra Inisiatif Siswazah (GP-IPS/2023/9737200), Welsh Government and a Sêr Cymru Strategic Partner Acceleration Award (80761-SU-242), the National Natural Science Foundation of China (W2533071). We would like to thank Shenzhen Shuyan Calculation Tech Co., Ltd for technical support with the molecular docking.

References

1. G. Moreno-Alcántar, P. Picchetti and A. Casini, *Angew Chem Int Ed*, 2023, **62**, e202218000.
2. S. Sen, M. Won, M. S. Levine, Y. Noh, A. C. Sedgwick, J. S. Kim, J. L. Sessler and J. F. Arambula, *Chem Soc Rev*, 2022, **51**, 1212-1233.

3. Q. Peña, A. Wang, O. Zaremba, Y. Shi, H. W. Scheeren, J. M. Metselaar, F. Kiessling, R. M. Pallares, S. Wuttke and T. Lammers, *Chem Soc Rev*, 2022, **51**, 2544-2582.
4. L. Gourdon, K. Cariou and G. Gasser, *Chem Soc Rev*, 2022, **51**, 1167-1195.
5. C.-P. Tan, Y.-M. Zhong, L.-N. Ji and Z.-W. Mao, *Chem Sci*, 2021, **12**, 2357-2367.
6. F. E. Poynton, S. A. Bright, S. Blasco, D. C. Williams, J. M. Kelly and T. Gunnlaugsson, *Chem Soc Rev*, 2017, **46**, 7706-7756.
7. L. Zeng, P. Gupta, Y. Chen, E. Wang, L. Ji, H. Chao and Z.-S. Chen, *Chem Soc Rev*, 2017, **46**, 5771-5804.
8. M. Martínez-Alonso and G. Gasser, *Coord Chem Rev*, 2021, **434**, 213736.
9. A. Notaro and G. Gasser, *Chem Soc Rev*, 2017, **46**, 7317-7337.
10. A. Rilak Simović, R. Masnikosa, I. Bratsos and E. Alessio, *Coord Chem Rev*, 2019, **398**, 113011.
11. N. A. Yusoh, M. R. Gill and X. Tian, *Chem Soc Rev*, 2025, **54**, 3616-3646.
12. G. Li, L. Sun, L. Ji and H. Chao, *Dalton Trans*, 2016, **45**, 13261-13276.
13. K. Lin, Z.-Z. Zhao, H.-B. Bo, X.-J. Hao and J.-Q. Wang, *Front Pharmacol*, 2018, **9**.
14. M. R. Gill, J. Garcia-Lara, S. J. Foster, C. Smythe, G. Battaglia and J. A. Thomas, *Nat Chem*, 2009, **1**, 662-667.
15. Z. Chen, F. Han, Y. Du, H. Shi and W. Zhou, *Signal Transduct Target Ther*, 2023, **8**, 70.
16. K. Nepali, H.-Y. Lee and J.-P. Liou, *J Med Chem*, 2019, **62**, 2851-2893.
17. S. Qi, Z. Jin, Y. Jian, Y. Hou, C. Li, Y. Zhao, X. Wang and Q. Zhou, *Chemical Communications*, 2021, **57**, 4162-4165.
18. A. B. Becceneri, M. T. Martin, A. E. Graminha, M. R. Cominetti, P. C. Ford and R. Santana da Silva, *Dalton Transactions*, 2024, **53**, 11264-11275.

19. G. L. Sasahara, F. S. Gouveia Júnior, R. O. Rodrigues, D. S. Zampieri, S. Fonseca, R. C. R. Gonçalves, B. R. Athaydes, R. R. Kitagawa, F. A. Santos, E. H. S. Sousa, A. T. Nagao-Dias and L. G. F. Lopes, *J Inorg Biochem*, 2020, **206**, 111048.
20. H. Jin, L. Wang and R. Bernards, *Nat Rev Drug Discov*, 2023, **22**, 213-234.
21. R. B. Mokhtari, T. S. Homayouni, N. Baluch, E. Morgatskaya, S. Kumar, B. Das and H. Yeger, *Oncotarget*, 2017, **8**, 38022-38043.
22. N. A. Yusoh, H. Ahmad and M. R. Gill, *ChemMedChem*, 2020, **15**, 2121-2135.
23. N. A. Yusoh, H. Ahmad, K. A. Vallis and M. R. Gill, *Med Oncol*, 2025, **42**, 262.
24. N. A. Yusoh, S. L. Chia, N. Saad, H. Ahmad and M. R. Gill, *Sci Rep*, 2023, **13**, 1456.
25. N. A. Yusoh, S. W. Leong, S. L. Chia, S. N. Harun, M. B. A. Rahman, K. A. Vallis, M. R. Gill and H. Ahmad, *ACS Chem Biol*, 2020, **15**, 378-387.
26. S. Leijen, S. A. Burgers, P. Baas, D. Pluim, M. Tibben, E. van Werkhoven, E. Alessio, G. Sava, J. H. Beijnen and J. H. Schellens, *Invest New Drugs*, 2015, **33**, 201-214.
27. K. Lin, Y. Rong, D. Chen, Z. Zhao, H. Bo, A. Qiao, X. Hao and J. Wang, *Front Oncol*, 2020, **10**, 141.
28. A. Bergamo, T. Riedel, P. J. Dyson and G. Sava, *Invest New Drugs*, 2015, **33**, 53-63.
29. P. Heffeter, B. Atil, K. Kryeziu, D. Groza, G. Koellensperger, W. Körner, U. Jungwirth, T. Mohr, B. K. Keppler and W. Berger, *Eur J Cancer*, 2013, **49**, 3366-3375.
30. R. H. Berndsen, A. Weiss, U. K. Abdul, T. J. Wong, P. Meraldi, A. W. Griffioen, P. J. Dyson and P. Nowak-Sliwinska, *Sci Rep*, 2017, **7**, 43005.
31. D. Sharma, F. Rasool, M. Bharti, K. M. Vyas and S. K. J. Magani, *Int J Mol Sci*, 2023, **24**, 686.
32. D. Chen, S. Guo, X. Tang, Y. Rong, H. Bo, H. Shen, Z. Zhao, A. Qiao, J. Shen and J. Wang, *J Inorg Biochem*, 2022, **230**, 111749.

33. L. Mei, J. Zhang, K. He and J. Zhang, *J Hematol Oncol*, 2019, **12**, 43.
34. E. Fokas, R. Prevo, E. M. Hammond, T. B. Brunner, W. G. McKenna and R. J. Muschel, *Cancer Treat Rev*, 2014, **40**, 109-117.
35. N. Y. L. Ngoi, P. G. Pilié, D. J. McGrail, M. Zimmermann, K. Schlacher and T. A. Yap, *Nat Rev Clin Oncol*, 2024, **21**, 278-293.
36. S. Stockton, C. Shyr, M. Cecchini, R. Aljumaily, T. R. Halfdanarson, M. B. Sonbol, J. Whisenant, S. P. Ivy, P. LoRusso, S. Das, S. Gore, J. Berlin, J. H. Beumer and T. R. Heumann, *J Clin Oncol*, 2024, **42**, 3076-3076.
37. H. A. Burris, J. Berlin, T. Arkenau, G. M. Cote, M. P. Lolkema, J. Ferrer-Playan, A. Kalapur, J. Bolleddula, G. Locatelli, T. Goddemeier, I. Gounaris and J. de Bono, *Br J Cancer*, 2024, **130**, 1131-1140.
38. U. Jo, Y. Arakawa, A. Zimmermann, D. Taniyama, M. Mizunuma, L. M. Jenkins, T. K. Maity, S. Kumar, F. T. Zenke, N. Takebe and Y. Pommier, *Mol Cancer Ther*, 2024, **23**, 911-923.
39. S. Banerjee, J. Stewart, N. Porta, C. Toms, A. Leary, S. Lheureux, S. Khalique, J. Tai, A. Attygalle, K. Vroobel, C. J. Lord, R. Natrajan and J. Bliss, *Int J Gynecol Cancer*, 2021, **31**, 1471-1475.
40. H. Mahdi, N. Hafez, D. Doroshow, D. Sohal, V. Keedy, K. T. Do, P. LoRusso, J. Jürgensmeier, M. Avedissian, J. Sklar, C. Glover, B. Felicetti, E. Dean, P. Mortimer, G. I. Shapiro and J. P. Eder, *JCO Precis Oncol*, 2021, **5**.
41. P. D. Shah, S. L. Wethington, C. Pagan, N. Latif, J. Tanyi, L. P. Martin, M. Morgan, R. A. Burger, A. Haggerty, H. Zarrin, D. Rodriguez, S. Domchek, R. Drapkin, I. M. Shih, S. A. Smith, E. Dean, S. Gaillard, D. Armstrong, D. A. Torigian, W. T. Hwang, R. Giuntoli and F. Simpkins, *Gynecol Oncol*, 2021, **163**, 246-253.

678 42. H. Kim, H. Xu, E. George, D. Hallberg, S. Kumar, V. Jagannathan, S. Medvedev, Y. Kinose,
679 K. Devins, P. Verma, K. Ly, Y. Wang, R. A. Greenberg, L. Schwartz, N. Johnson, R. B. Scharpf,
680 G. B. Mills, R. Zhang, V. E. Velculescu, E. J. Brown and F. Simpkins, *Nat Commun*, 2020, **11**,
681 3726.
682 43. M. R. Gill, S. N. Harun, S. Halder, R. A. Boghozian, K. Ramadan, H. Ahmad and K. A. Vallis,
683 *Sci Rep*, 2016, **6**, 31973.
684 44. A. M. Weber and A. J. Ryan, *Pharmacology & Therapeutics*, 2015, **149**, 124-138.
685 45. J. Liu, W. J. Mei, L. J. Lin, K. C. Zheng, H. Chao, F. C. Yun and L. N. Ji, *Inorg Chim Acta*, 2004,
686 **357**, 285-293.
687 46. M. R. Gill, D. Cecchin, M. G. Walker, R. S. Mulla, G. Battaglia, C. Smythe and J. A. Thomas,
688 *Chem Sci*, 2013, **4**, 4512-4519.
689 47. M. Chauhan, K. Banerjee and F. Arjmand, *Inorg Chem*, 2007, **46**, 3072-3082.
690 48. J. R. Lakowicz and G. Weber, *Biochem*, 1973, **12**, 4161-4170.
691 49. T.-C. Chou and P. Talalay, *Trends Pharmacol Sci*, 1983, **4**, 450-454.
692 50. T.-C. Chou and P. Talalay, *Adv Enzyme Regul*, 1984, **22**, 27-55.
693 51. U. S. Srinivas, B. W. Q. Tan, B. A. Vellayappan and A. D. Jeyasekharan, *Redox Biol*, 2019,
694 **25**, 101084.
695 52. M. S. Costa, Y. G. Gonçalves, B. C. Borges, M. J. B. Silva, M. K. Amstalden, T. R. Costa, L. M.
696 G. Antunes, R. S. Rodrigues, V. d. M. Rodrigues, E. de Faria Franca, M. A. P. Zoia, T. G. de
697 Araújo, L. R. Goulart, G. Von Poelhsitz and K. A. G. Yoneyama, *Scientific Reports*, 2020, **10**,
698 15410.

699 53. G. Á. Ferreira-Silva, C. C. Candido, G. Y. Garavelli, C. Girotto Pressete, E. S. Caixeta, A. E.
700 Graminha, M. I. F. Barbosa, A. C. Doriguetto, M. Ionta and A. Ferro Aissa, *ACS Omega*,
701 2025, **10**, 28956-28968.
702 54. J. Karges, S. Kuang, F. Maschietto, O. Blacque, I. Ciofini, H. Chao and G. Gasser, *Nat*
703 *Commun*, 2020, **11**, 3262.
704 55. K. M. Johnson, Z. D. Parsons, C. L. Barnes and K. S. Gates, *J Org Chem*, 2014, **79**, 7520-
705 7531.
706 56. X. Shen, C. H. Laber, U. Sarkar, F. Galazzi, K. M. Johnson, N. G. Mahieu, R. Hillebrand, T.
707 Fuchs-Knotts, C. L. Barnes, G. A. Baker and K. S. Gates, *J Org Chem*, 2018, **83**, 3126-3131.
708 57. C. Braga, M. Ferreira-Silva, M. L. Corvo, R. Moreira, A. R. Fernandes, J. Vaz and M. J. Perry,
709 *RSC Med Chem*, 2025, DOI: 10.1039/d4md00876f.
710 58. Y. Han, W. Chen, Y. Kuang, H. Sun, Z. Wang and X. Peng, *Chem Res Toxicol*, 2015, **28**, 919-
711 926.
712 59. J. Wang, T. Ren, G. Sun, N. Zhang, L. Zhao and R. Zhong, *Int J Biol Macromol*, 2025, **319**,
713 145344.
714 60. B. Fernández, I. Fernández, J. Cepeda, M. Medina-O'Donnell, E. E. Rufino-Palomares, Á.
715 Raya-Barón, S. Gómez-Ruiz, A. Pérez-Jiménez, J. A. Lupiáñez, F. J. Reyes-Zurita and A.
716 Rodríguez-Diéguez, *Cryst Growth Des*, 2018, **18**, 969-978.
717 61. F. M. Barnieh, P. M. Loadman and R. A. Falconer, *Curr Res Pharmacol Drug Discov*, 2021,
718 **2**, 100017.
719 62. J. J. Deppas, B. F. Kiesel, J. Guo, L. H. Rigatti, J. D. Latoche, A. Green, P. Knizner, D. A. Clump,
720 P. Pandya, F. P. Vendetti, C. J. Bakkenist and J. H. Beumer, *Toxicol Appl Pharmacol*, 2025,
721 **500**, 117375.

63. S. Höfer, L. Frasch, S. Brajkovic, K. Putzker, J. Lewis, H. Schürmann, V. Leone, A. Sakhteman, M. The, F. P. Bayer, J. Müller, F. Hamood, J. T. Siveke, M. Reichert and B. Kuster, *Mol Syst Biol*, 2025, **21**, 231-253.
64. H. Zhang, J. Kreis, S.-E. Schelhorn, H. Dahmen, T. Grombacher, M. Zühlsdorf, F. T. Zenke and Y. Guan, *Nat Commun*, 2023, **14**, 8310.
65. K. J. Herbert, R. Upstill-Goddard, S. B. Dreyer, S. Rebus, C. Pilarsky, M. Debabrata, C. J. Lord, A. V. Biankin, F. E. M. Froeling and D. K. Chang, *Br J Cancer*, 2025, **133**, 381-393.